
Abstract

Theoretical condensed matter research is plagued by a fundamental issue of complexity. The sheer amount of degrees of freedom in a material on any technologically relevant scale is overwhelming (e.g. $\sim 10^{23}$ electrons per cm^3), and makes it impossible to describe the quantum mechanical wavefunction exactly.

The Hamiltonian plays a central role in the description of crystals, the subject of this thesis. It can be decomposed into various parts, and their interactions. Depending on the physics under scrutiny it then often suffices to solve only one of those parts. This can be either because the energy scales and associated timescales that govern the constituents are very different, or because the interactions between them are small. One example, often put into practice, is the separation of electronic and phononic (lattice) degrees of freedom, leading to the well-known Born-Oppenheimer approximation, decoupling their respective motion. Another is the often neglected spin-orbit coupling, due to the tiny prefactor associated with its relativistic origin.

Solving these subproblems then allows for progress to be made in understanding the physics that govern them. However, there will inevitably be systems for which this interaction is not small and leads to fascinating new physics that manifestly depends on both subsystems combined. In this thesis we focus on these cases and how they arise in functional materials, with the occasional eye towards applications in technology.

The reason why these cross-order couplings can be interesting for technological applications, is that often one of the orders is more robust with respect to perturbations, and therefore more long-lived, but also harder to control efficiently. By exploiting the cross-order coupling in certain materials, one could potentially control the long lived order by applying perturbations to the more easily controllable order.

In giant Rashba effect systems, the coupling between spin and ferroelectric order leads to a linear spin-splitting of the band structure, whose sign depends on the orientation of the ferroelectric polarization. We show that, rather than the relativistic Rashba effect, a combination of electrostatics and atomic spin-orbit coupling lies at the origin of the large splitting.

The coupling between magnetism and ferroelectricity in multiferroic GdMn_2O_5 leads to a never before observed four-state hysteresis loop for the ferroelectric polarization, which depends on the magnitude, angle and history of the applied magnetic field. As we will show, this four-state hysteresis loop is accompanied by a full 360° rotation of spins in the material, which resembles the crankshaft of a car, converting the linear back-and-forth motion of the magnetic field into a rotational motion of the spins.

In a thin film of elemental Chromium, the ultrafast dynamics of a spin density wave, coupled to a slower varying charge density wave, allows for a high degree of control of the latter through excitations of the former. This allows us to predict the sequence of optical pulses to be applied to the material in order to follow closely an enveloping signal function.

And finally, the coupling between ferroelectricity and strain in BaTiO_3 leads to a softening at purely ferroelectric domain walls, allowing for some mechanical control of the position of this wall.

We utilize both theoretical and computational tools to understand the nature of these interactions, how they lead to cross-order coupling in these materials, and how this then translates into the experimentally observed behavior.

Contents

1	Theory	5
1.1	Spin-orbit coupling	5
1.2	Wannier Functions	5
2	Spin-momentum locking in high spin-orbit coupled ferroelectrics	11
2.1	Introduction	11
2.2	Rashba-Bychkov Effect	12
2.3	Orbital Rashba Effect	15
2.3.1	Tight-Binding model	15
2.4	Overview: Germanium Telluride	19
2.5	Methods	20
2.6	Band structure	21
2.7	Results and Discussion	22
2.8	Conclusions	23

Chapter 1

Theory

1.1 Spin-orbit coupling

1.2 Wannier Functions

In a lot of the work presented in this Thesis we construct simplified model Hamiltonians to try and describe the physics that are manifested real materials. For topics involving the electronic structure, either directly in describing the Rashba-splitting of energy bands in Chapter 2, or indirectly to parametrize the magnetic exchanges between localized spins as in Chapter ??, tight-binding models are often the most appropriate tool. These are constructed by defining a localized, often atomic-like, set of orbitals which is repeated inside each unit cell, and the so-called hopping terms between them. The first benefit of this simplification is that it makes the numerics of the problem more tractable, since a limited set of orbitals leads to small dimensions of the matrices that represent various operators. Secondly, the representation in terms of real-space localized wavefunctions, as compared with the extended Bloch functions (BFs) that diagonalize the Hamiltonian, often also leads to a more intuitive picture. There are two main methods that are used to construct the tight-binding Hamiltonian. The first is to use a semi-empirical approach, where first a set of localized orbitals is chosen, in terms of which the elements of the Hamiltonian can be written down as a combination of certain model parameters, the amount of which is reduced by using symmetry arguments. In the case of real materials one then uses experimental measurements to fit these model parameters.

The second is to extract these orbitals, and parameters from a first-principles based simulation such as density functional theory. In thesis we favor the latter since it is more flexible, not depending on experiments while still providing quantitative results. This also allows for an easy comparison of multiple materials in order to better understand how certain physics manifest themselves in different cases.

The main question to answer then becomes how to define a such a set of localized orbitals, when most simulations for periodic systems handle extended BFs $|\psi^k(\mathbf{r})\rangle = e^{i\mathbf{k}\cdot\mathbf{r}} u^k(\mathbf{r})$, where \mathbf{k} denotes a wavevector in the first Brillouin zone (BZ), $e^{i\mathbf{k}\cdot\mathbf{r}}$ the plane wave envelope function, and $u^k(\mathbf{r})$ the cell-periodic part (see the left panel of Fig. 1.1(a)). There are many ways to do this, but the most natural one in this case is that of the Wannier functions (WFs) [Wannier1937].

We will here give a short recap of the excellent review done by Marzari et. al.

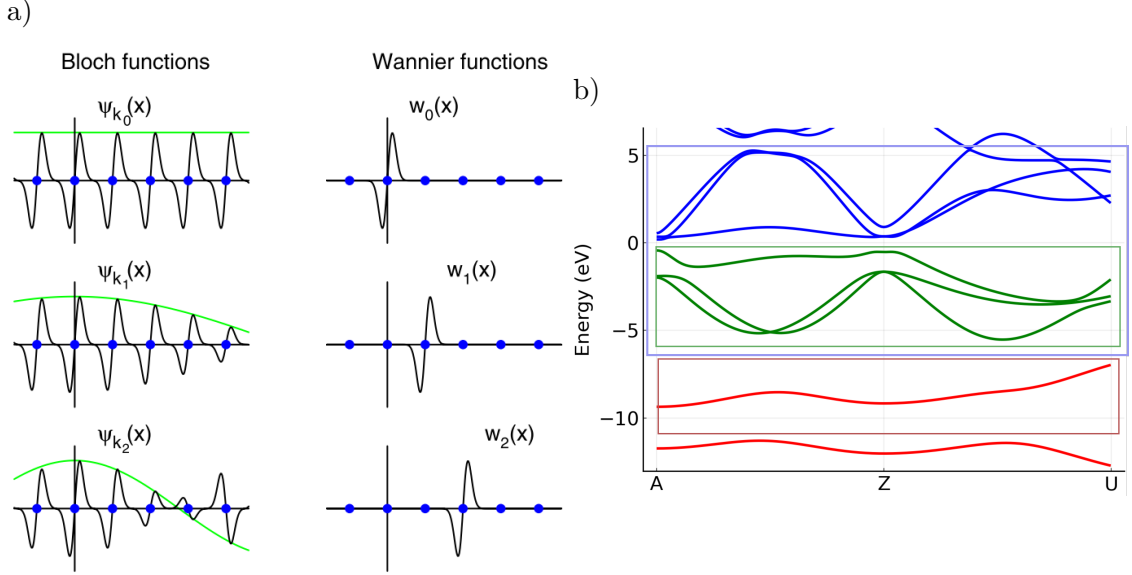


Figure 1.1: a) A comparison between Bloch functions (left) and Wannier functions (right). The green line in the left panel denotes the envelope function $e^{ik \cdot r}$. b) Bandstructure of semiconductor GeTe, demonstrating three cases for Wannierization: red is a single disconnected band, green shows a disconnected composite manifold of connected bands, blue shows the situation when bands need to be disentangled.

[Marzari2012], starting with the most clear case of a single isolated band n with BFs $|\psi_n^{\mathbf{k}}(\mathbf{r})\rangle$ (see red window in Fig. 1.1(b)), where the BF can be written as a straightforward discrete Fourier transform of the WF:

$$|\psi_n^{\mathbf{k}}(\mathbf{r})\rangle = e^{i\mathbf{k} \cdot \mathbf{r}} |u_n^{\mathbf{k}}(\mathbf{r})\rangle = \sum_{\mathbf{R}} e^{i\mathbf{k} \cdot \mathbf{R}} |w_n^{\mathbf{R}}(\mathbf{r})\rangle, \quad (1.1)$$

with $|u_n^{\mathbf{k}}(\mathbf{r})\rangle$ the periodic part of the BF, $|w_n^{\mathbf{R}}(\mathbf{r})\rangle$ the localized WF centered in the unit cell defined by lattice vector \mathbf{R} , and n the band index. The comparison between BFs and WFs is made in Fig. 1.1. When $k = 0$ we can see that the periodic part of the BF $u_n^{\mathbf{k}}(\mathbf{r})$ is simply the sum over the WFs centered at different unit cells. In the case of $k \neq 0$, similar to how the envelope part modulates the periodic part of the BF, the contribution of each WF to the total sum needs to be modulated in a discrete way through $e^{i\mathbf{k} \cdot \mathbf{R}}$.

The inverse Fourier transform over the BF in the first Brillouin Zone (BZ) can then be performed in order to generate the localized WFs,

$$|w_n^{\mathbf{R}}(\mathbf{r})\rangle = \frac{V}{(2\pi)^3} \int_{BZ} d\mathbf{k} e^{-i\mathbf{k} \cdot \mathbf{R}} |\psi_n^{\mathbf{k}}(\mathbf{r})\rangle, \quad (1.2)$$

where V denotes the real-space volume of the unit cell. In these and following equations, the normalization convention is used such that $\int_V d\mathbf{r} \langle \psi_n^{\mathbf{k}}(\mathbf{r}) | \psi_n^{\mathbf{k}}(\mathbf{r}) \rangle = 1$. As can be seen from the right panel in Fig. 1.1, WFs centered in different unit cells are shifted copies of one another.

One of the most useful properties of the WFs lies in the realization that, through the gauge freedom at each \mathbf{k} of the BF¹, the shape of the WFs is not unique:

$$|\psi_n^{\mathbf{k}}(\mathbf{r})\rangle \Rightarrow |\tilde{\psi}_n^{\mathbf{k}}(\mathbf{r})\rangle = e^{i\phi_n^{\mathbf{k}}} |\psi_n^{\mathbf{k}}(\mathbf{r})\rangle \quad (1.3)$$

$$|w_n^{\mathbf{R}}(\mathbf{r})\rangle \Rightarrow |\tilde{w}_n^{\mathbf{R}}(\mathbf{r})\rangle = \frac{V}{(2\pi)^3} \int_{BZ} d\mathbf{k} e^{-i(\mathbf{k}\cdot\mathbf{R}+\phi_n^{\mathbf{k}})} |\psi_n^{\mathbf{k}}(\mathbf{r})\rangle, \quad (1.4)$$

This means that by varying $\phi_n^{\mathbf{k}}$ we can adapt the WF basis to the needs of the particular problem under investigation. In the case of a single isolated band this is a bonafide luxury exploitable to simplify the task at hand. However, in pretty much all practical problems, it are groups of bands that we are interested in. The simplest case is when these form a composite manifold that is detached from other bands, such as the green valence bands in Fig. 1.1(b).

It is natural to generalize the notion of the single band gauge transformation (in that case amounting to a single free phase), to this manifold of states:

$$|\tilde{\psi}_m^{\mathbf{k}}(\mathbf{r})\rangle = \sum_m U_{nm}^{\mathbf{k}} |\psi_n^{\mathbf{k}}(\mathbf{r})\rangle. \quad (1.5)$$

Here n, m are band indices enumerating the bands inside the composite manifold. These transformed states are no longer eigenstates of the Hamiltonian if $U_{nm}^{\mathbf{k}}$ has off-diagonal elements. Traces performed over such an isolated set of bands are invariant w.r.t. to these gauge transformations, leading to the invariance of observables such as the Hamiltonian which lies at the core of the ability to isolate and focus on this subproblem. Choosing right gauge is a necessity in order to extract well localized WFs, however, because composite band manifolds, in general, will harbor crossings and degeneracies where the BFs become non-analytic and thus the variation of the periodic parts $u_n^{\mathbf{k}}(\mathbf{r})$ will not be smooth in the variation over \mathbf{k} . This is an issue, since it is a well known fact that only smooth functions in reciprocal space lead to well localized ones in real space when the inverse Fourier transform is performed. Indeed, in Eq. 1.2, only then will there be a cancellation of the terms from the fast varying exponent $e^{i\mathbf{k}\cdot\mathbf{R}}$ when \mathbf{R} becomes large. It is thus important to choose a gauge at each k -point such that the rotated wavefunctions $|\tilde{\psi}_n^{\mathbf{k}}(\mathbf{r})\rangle$ vary as smoothly as possible, which will ultimately lead to the WFs that are as localized as possible². The localization functional can be written down as

$$\Omega = \sum_n \langle w_n^0 | r^2 | w_n^0 \rangle - |\langle w_n^0 | \mathbf{r} | w_n^0 \rangle|^2. \quad (1.6)$$

¹The solution to Schrödinger equation does not determine uniquely its phase.

²It can be proved that these WFs will be exponentially localized in the case of normal insulators.

This can be split up into a gauge-invariant and gauge-dependent part

$$\Omega = \Omega_I + \tilde{\Omega}, \quad (1.7)$$

$$\Omega_I = \sum_n \left[\langle w_n^0 | r^2 | w_n^0 \rangle - \sum_{m, \mathbf{R}} |\langle w_m^{\mathbf{R}} | \mathbf{r} | w_n^0 \rangle|^2 \right] \quad (1.8)$$

$$\tilde{\Omega} = \sum_n \sum_{m, \mathbf{R} \neq n, 0} |\langle w_m^{\mathbf{R}} | \mathbf{r} | w_n^0 \rangle|^2. \quad (1.9)$$

For a set of isolated bands it thus suffices to minimize the gauge-dependent part in order to find the unique set of maximally localized Wannier functions (MLFW) that constitute these bands [**Kunes2004, Marzari2012**]. We can write down the position dependent operators in reciprocal space as [**Blount1962**]

$$\langle w_n^{\mathbf{R}} | \mathbf{r} | w_m^0 \rangle = i \frac{V}{(2\pi)^3} \int d\mathbf{k} e^{i\mathbf{k} \cdot \mathbf{R}} \langle u_n^{\mathbf{k}} | \nabla_{\mathbf{k}} | u_m^{\mathbf{k}} \rangle \quad (1.10)$$

and

$$\langle w_n^{\mathbf{R}} | r^2 | w_m^0 \rangle = -\frac{V}{(2\pi)^3} \int d\mathbf{k} e^{i\mathbf{k} \cdot \mathbf{R}} \langle u_n^{\mathbf{k}} | \nabla_{\mathbf{k}}^2 | u_m^{\mathbf{k}} \rangle. \quad (1.11)$$

By then minimizing $\tilde{\Omega}$ in terms of different gauge transformations $U_{nm}^{\mathbf{k}}$ applied to the $|u_n^{\mathbf{k}}\rangle$, we can find a set of MLFW.

If maximal localization is not the goal, tweaking the $U_{nm}^{\mathbf{k}}$ allows for the generation of WFs with other desirable characteristics in a way that, e.g., they obey certain ionic-site symmetries. This can be achieved by projecting onto atomic-like orbitals, which can be very useful in gaining a further understanding in terms of orbitals with definite and known properties. More details on the different construction methods and can be found in Ref. [**Marzari2012**].

Up to now, only isolated sets of bands were discussed. However, in many cases such a set does not exist in the region of interest. This leads to sets of band which are termed *entangled*, being connected to bands that lie outside this energy range (see the blue bands in Fig. 1.1(b)). If we are seeking J WFs, we thus need to somehow select at each k -point J states $|\tilde{\psi}_n^{\mathbf{k}}(\mathbf{r})\rangle$ from a bigger set $J^{\mathbf{k}}$, that can then be used in the above described localization procedure:

$$|\tilde{\psi}_n^{\mathbf{k}}(\mathbf{r})\rangle = \sum_{m=1}^{J^{\mathbf{k}}} V_{nm}^{\mathbf{k}} |\psi_m^{\mathbf{k}}(\mathbf{r})\rangle. \quad (1.12)$$

$V_{nm}^{\mathbf{k}}$ are rectangular matrices of dimension $J \times J^{\mathbf{k}}$. This leads to a two-step process where first a subspace is selected for each k -point, followed by the final gauge selection to arrive at the final localized WFs.

$$|w_n^{\mathbf{R}}(\mathbf{r})\rangle = \frac{V}{(2\pi)^3} \int_{BZ} d\mathbf{k} e^{-i\mathbf{k} \cdot \mathbf{R}} \sum_{m=1}^J U_{\mathbf{k}}^{nm} \sum_{l=1}^{J^{\mathbf{k}}} V_{ml}^{\mathbf{k}} |\psi_l^{\mathbf{k}}(\mathbf{r})\rangle \quad (1.13)$$

There are again many ways to do this subspace selection (or *disentanglement*). The most prevalent two are to use another projection based method, or one that again focuses on minimizing the real space spread of the WFs. We utilize the latter in this work. It is based on finding the V_{nm}^k that lead to the maximal overlap of the selected subspaces with their neighbors at each k -point. The matrices will be generally rectangular in this case, since they transform a set of J^k wavefunctions into a smaller one with only J wavefunctions. As discussed before, this smoothness in reciprocal space translates into the subspace as a whole being more localized in real space. Indeed, it can be shown [Marzari2012] that this intrinsic smoothness is exactly what Ω_I measures in Eq. 1.8. Following this disentanglement procedure, we can apply the procedures described for the isolated manifold of bands to ultimately lead to the WFs which are very well localized. In many cases, it is also desirable to adapt the algorithm in such a way that the BFs inside a “frozen” energy window are exactly interpolated by the resulting WF base and tight-binding Hamiltonian.

In the previous equations a continuous integration over the BZ was performed for the fourier transform from BFs to WFs, however, in reality a discrete k -grid and Fourier transform is used. To keep close to the continuous case, the Fourier transform pair is defined as

$$\left| \tilde{\psi}_n^k(\mathbf{r}) \right\rangle = \sum_{\mathbf{R}} e^{i\mathbf{k}\cdot\mathbf{R}} \left| w_n^{\mathbf{R}}(\mathbf{r}) \right\rangle, \quad (1.14)$$

$$\left| w_n^{\mathbf{R}}(\mathbf{r}) \right\rangle = \frac{1}{N} \sum_{\mathbf{k}} e^{-i\mathbf{k}\cdot\mathbf{R}} \left| \tilde{\psi}_n^k(\mathbf{r}) \right\rangle, \quad (1.15)$$

where N denotes the number of unit cells in the periodic supercell in real space, or the number of k -points in the discrete mesh over the BZ. This discretization enforces periodic boundary conditions on the BFs over this supercell, meaning that the WFs in this definition also have this supercell periodicity. The localization then means that inside the supercell the WFs are localized. If the interpolation is continuous, the supercell is infinite, restoring the earlier definitions and original notion of WFs.

The final process to extract a tight-binding Hamiltonian in a WF basis, starting from an ab-initio DFT simulation, can thus be summarized as follows:

1. perform a self-consistent DFT calculation in order to find the ground state density and BFs over a discrete k -mesh to be used in the Wannierization
2. find which trial orbitals (e.g. atomic-like) are most suitable for the bands or problem under investigation. This can be done for example by performing a projected density of states calculation.
3. select an inner “frozen” window with the most important bands, and, if entangled, and an outer window from which to disentangle J -dimensional subspaces for each k -point

4. use a projection on the trial orbitals as the initial guess and then optimize the smoothness of the subspaces as a whole to find V_{ml}^k matrices to identify the J -dimensional subspaces.
5. find the final gauges U_{nm}^k in order to minimize the spread of each of the J WFs.

Further details on the Wannierization process can be found in Ref. [Marzari2012], and specific details on the implementation in the Wannier90 package used throughout this work can be found in Ref. [Mostofi2014AnFunctions].

When the U^k and V^k matrices are found, any property $f(\mathbf{k})$ defined on the k -mesh in terms of the BFs used in the first-principles calculation can be transformed into $F(\mathbf{R})$ in the Wannier representation. Since the WFs are well localized, $F(\mathbf{R})$ tends to decay rapidly with $|\mathbf{R}|$. It is important to realize that, depending on the coarseness of the k -grid used in the first-principles calculation, $F(\mathbf{R})$ can only be calculated for limited values of $|\mathbf{R}|$, spanning the supercell defined by the discretization of the BZ. Using these short-ranged real-space $F(\mathbf{R})$, it is then possible to interpolate the values of $f(\mathbf{k})$ by performing the inverse procedure. This allows to efficiently calculate $f(\mathbf{k})$ on a finer k -mesh compared with the one used in the first-principles calculations, provided the WFs are well localized inside the supercell defined by the original coarse k -mesh. This efficient interpolation is one of the great advantages of using this technique, since the basis, and thus dimensions of the matrices, is much lower than that used in the first-principles calculation (e.g. many plane waves).

The main quantity we will use this interpolation for is the Hamiltonian:

$$\tilde{H}_{nm}^k = \left\langle \tilde{\psi}_n^k(\mathbf{r}) \right| H \left| \tilde{\psi}_m^k(\mathbf{r}) \right\rangle = \sum_{\mathbf{R}} e^{i\mathbf{k}\cdot\mathbf{R}} \langle w_n^0 | H | w_n^{\mathbf{R}} \rangle, \quad (1.16)$$

where the tilde is used to distinguish the k -space wavefunctions from BFs, and $|w_n^{\mathbf{R}}\rangle$ denote the WFs centered at unit cell identified by lattice translation \mathbf{R} . To recover the bandstructure from this Hamiltonian can then be diagonalized by unitary transformations W^k such that

$$H_{nm}^k = [W^{k\dagger} \tilde{H}_{nm}^k W^k]_{nm} = \delta_{nm} \varepsilon_n^k. \quad (1.17)$$

This concludes this very condensed introduction and overview of the use and construction of Wannier functions as a tool to aid in the theoretical understanding of the behavior of electrons in extended systems.

Chapter 2

Spin-momentum locking in high spin-orbit coupled ferroelectrics

2.1 Introduction

The research field of spintronics aims to understand the behavior of spins inside materials, and translate this understanding into active control of these degrees of freedom for possible technological applications. Many possible devices have been theorized, for example, spin field-effect transistors (spin-FET)[**Datta1990**], and storage devices which utilize spin-current and associated spin-transfer torque to efficiently manipulate magnetic domains [**Kent2015, Jungwirth2016**]. In spite of fundamental interest and potential for applications, the actual realization of these devices has been rather elusive. One of the main culprits for the limited success to date is that the devices require very granular, ideally electric, control of the spin. This is often precluded by the widely separated energy scales and weak coupling between magnetic and charge degrees of freedom. One class of materials that can allow for such electric control of spin-polarized states are the ferroelectric semiconductors with large atomic spin-orbit coupling (SOC) [**DiSante2013, Ishizaka2011, Kim2014**]. Inversion symmetry breaking together with SOC results in a linear energy splitting of spin-polarized bands, manifested in the band structure as a conical intersection surrounding a time-reversal symmetric point of the Brillouin Zone (BZ) (see Fig. 2.1). Due to the definite spin-polarization of these bands, current carriers¹ traveling through the material will tend to align their spins to this spin-polarization. As we discuss in more detail in the following, the direction of the spin polarization depends on the orientation and strength of the electric field \mathbf{E} . In ferroelectrics, an internal field results from the polarization P , allowing it to be tuned and switched by an external electric field. These spin-polarized states have been observed both experimentally [**Ishizaka2011, Liebmann2016, Krempasky2015SurfaceSemiconductor**], and from *ab-initio* density functional theory (DFT) simulations [**DiSante2013**]. It is, however, often not well understood and misattributed what the underlying microscopic mechanisms are that lead to the observed splitting.

We start by investigating multiple origins of this k and E dependent spin-splitting. The discussed energy contributions all arise due to the Hamiltonian of

¹holes in the case of Fig. 2.1

form

$$H_R(\mathbf{k}) = \alpha_R \frac{\mathbf{E}}{|\mathbf{E}|} \cdot (\mathbf{k} \times \hat{\sigma}), \quad (2.1)$$

where $\hat{\sigma}$ is the electron spin operator, and \mathbf{E} the electric field. It will turn out that multiple microscopic effects can lead to contributions of this form, some of these are well known, others are more obscure. The magnitude of the contribution depends on the microscopic origin, namely whether the effect is purely relativistic or rather a combination of relativistic and electrostatic terms.

Certain materials showcase an exceedingly big splitting, for example in GeTe as can be seen in Fig. 2.1, and we therefore use this material as the main example throughout this chapter. To investigate how these effects occur in GeTe, we utilize DFT, followed by a Wannierization, in order to investigate local real-space properties of the Bloch functions around the time reversal symmetric points of the BZ.

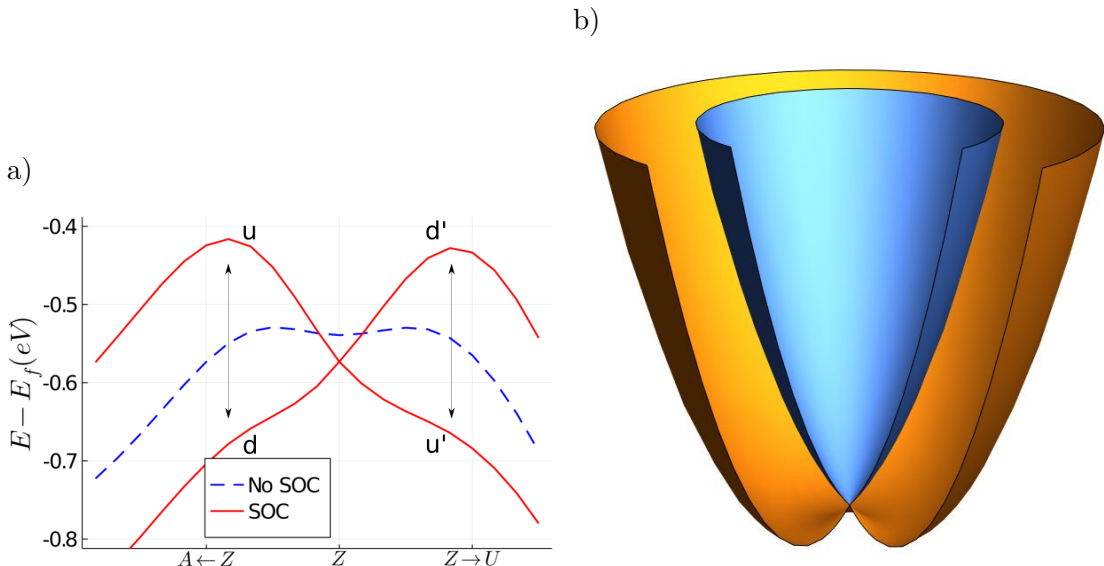


Figure 2.1: **Large Rashba splitting** (a) The band dispersion of the first valence band in GeTe, around the Z -point of the Brillouin zone (see Fig. 2.4 for details). Two graphs show both non spin-orbit coupled (NSOC, blue), and spin-orbit coupled (SOC, red) case. The $u-d$ and $u'-d'$ labels designate the up and down spin-polarized bands, where the prime signifies that the orientation of the spin axis depends on specific path followed in k -space. b) Shifted parabolic energy levels due to Rashba splitting, and associated spin texture.

We finish with a conclusion on the origin of most observed Rashba-like phenomena [could be better].

2.2 Rashba-Bychkov Effect

The first discovered and most well known effect bearing the form of Eq. 2.1 is the Rashba-Bychkov effect, first derived in their seminal 1959 paper [**Rashba1959SymmetryAr**].

It is a relativistic effect that is derived from an expansion to second order in $1/c$, c denoting the speed of light, of the electronic Dirac equation (where the Fouldy-Wouthuysen transformation was applied):

$$\mathcal{H}\psi = \left[\frac{\mathbf{p}^2}{2m} - eV - \frac{e\hbar}{4m^2c^2}(\boldsymbol{\sigma} \cdot [\nabla V \times \mathbf{p}]) - \frac{\hbar^2}{8m^2c^2}\Delta V - \frac{\mathbf{p}^4}{8m^3c^2} \right] \psi = E\psi \quad (2.2)$$

where ψ is a two component spinor, V denotes the electric potential, $\boldsymbol{\sigma}$ a vector of Pauli-matrices ($\sigma_x, \sigma_y, \sigma_z$), m and e the electron mass and charge respectively, and \mathbf{p} the canonical momentum. The first two terms are the nonrelativistic part of the Hamiltonian, the third represents the SOC, the fourth is known as the Darwin effect and the fifth is the relativistic correction to the effective electron mass. As is common in literature, we introduce the spin-orbit coupling constant $\lambda = \frac{e\hbar}{4m^2c^2}$. In a crystal with a periodic potential $V(\mathbf{r})$, electronic wavefunctions are Bloch wavefunctions $\psi_n(\mathbf{k}, \mathbf{r}) = u_n(\mathbf{k}, \mathbf{r})e^{i\mathbf{k}\cdot\mathbf{r}}$, where u_n denotes the cell-periodic part, and n is the band index. To obtain the eigenvalue equation for $u_n^k(\mathbf{r})$, we insert ψ_n in Eq. 2.2, and carry out the differentiation $\mathbf{p}e^{i\mathbf{k}\cdot\mathbf{r}}u_n(\mathbf{k}, \mathbf{r}) = e^{i\mathbf{k}\cdot\mathbf{r}}(\mathbf{p} + \mathbf{k})u_n(\mathbf{k}, \mathbf{r})$, and similarly $\mathbf{p}^2 \rightarrow (\mathbf{p} + \mathbf{k})^2$. This leads to the following equation for $u_n^k(\mathbf{r})$:

$$E_n u_n(\mathbf{k}, \mathbf{r}) = (V_0 + V_1 + V_2 + V_3) u_n(\mathbf{k}, \mathbf{r}) \quad (2.3)$$

$$V_0(\mathbf{k}) = \frac{\mathbf{p}^2}{2m} - eV + \frac{\hbar^2 k^2}{2m} \quad (2.4)$$

$$V_1(\mathbf{k}) = \hbar \frac{\mathbf{k} \cdot \mathbf{p}}{m} \quad (2.5)$$

$$V_2(\mathbf{k}) = -\lambda \boldsymbol{\sigma} \cdot (\nabla V \times \mathbf{k}) \quad (2.6)$$

$$V_3(\mathbf{k}) = -\lambda \boldsymbol{\sigma} \cdot (\nabla V \times \mathbf{p}). \quad (2.7)$$

We neglected the last two terms of Eq. 2.2 since they are exceedingly small and don't contribute to the linear form of Eq. 2.1. It is important to understand how the electric fields inside the crystal contribute to V_2 and V_3 , where both terms originate from the application of \mathbf{p} to either $u_n^k(\mathbf{r})$ or $e^{i\mathbf{k}\cdot\mathbf{r}}$, respectively. We first separate ∇V in two contributions, one coming from the potential wells created by the atoms, and another originating from the ferroelectric polarization (it is assumed that no external fields are applied):

$$\nabla V = \mathbf{E} = \mathbf{E}_{at} + \mathbf{E}_P \quad (2.8)$$

These contributions, together with the two parts of the Bloch functions (i.e. the cell periodic $u_n^k(\mathbf{r})$, and envelope function $e^{i\mathbf{k}\cdot\mathbf{r}}$) are pictorially shown in Fig. 2.2.

Looking at the picture, it becomes clear that the contribution of the atomic potential applied to the envelope function is zero because while k is a constant, E_{at} is odd throughout the unit cell, leading to the contributions on either side of the potential well to cancel out. Thus the only contribution to the first term in Eq. 2.9 comes from the uniform (even) E_P , which in general is very small compared to the

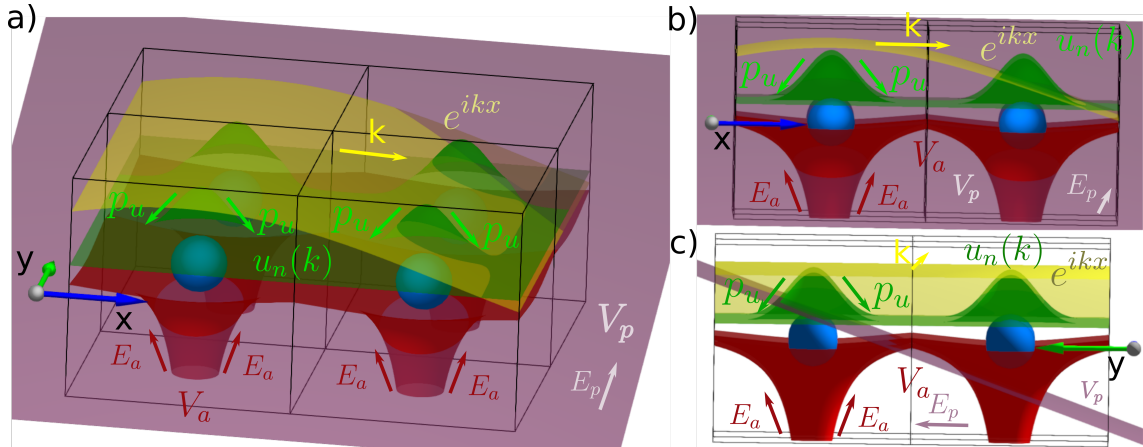


Figure 2.2: Pictorial representation of the different electric potentials (V) and fields (E) in a 2D square lattice. The blue spheres show the atoms, which produce the spherically symmetric red potential V_a and field E_a . The purple slab denotes a uniform ferroelectric polarization potential V_p which in this case is directed along the crystalline y -direction, creating field E_p . The green and yellow surfaces denote two components of the Bloch function: $u_n(k)e^{ikx}$, where the yellow is the envelope plane wave part and the green the cell periodic part. k and p_u denote the two components to the momentum of the bloch function, the former from the envelope function, and the latter the contribution from the periodic part.

atomic one. A similar argument can be applied to the contribution to V_3 . Due to the shape of the periodic part of the wavefunction, only the contribution coming from E_{at} will be nonzero, this is essentially the well-known atomic spin-orbit coupling and can be rather large.

In the following it is assumed that Eq. 2.3 can be solved for a time reversal (TR) invariant point \mathbf{k}_0 in the first BZ, where the two spin states are necessarily degenerate. Due to the broken inversion symmetry and inclusion of the SOC terms (V_2, V_3), this degeneracy will be broken for k points away from the TR invariant point. We denote the two degenerate states at \mathbf{k}_0 by $|u_n^\downarrow\rangle$ and $|u_n^\uparrow\rangle$. It is important to realize that the orientation of spin axis of the eigenstates of Eq. 2.3 depends on the direction of both \mathbf{k} and \mathbf{P} , as will become clear later. Without loss of generality we take $\mathbf{k}_0 = \mathbf{0}$ and $E_n^{\uparrow,\downarrow}(\mathbf{0}) = 0$. Expanding in the deviation away from the high-symmetry point, in the usual $\mathbf{k} \cdot \mathbf{p}$ sense, and keeping only linear \mathbf{k} terms and terms up to second order in $1/c$, we get

$$E_n^{\sigma_1}(\mathbf{k}) = -V_2^{\sigma_1}(\mathbf{k}) + \quad (2.9)$$

$$\sum_{m,\sigma_2 \neq n,\sigma_1} \frac{\langle u_n^{\sigma_1} | V_1(\mathbf{k}) | u_m^{\sigma_2} \rangle \langle u_m^{\sigma_2} | V_3(\mathbf{k}) | u_n^{\sigma_1} \rangle + h.c.}{E_n^{\sigma_1} - E_m^{\sigma_2}}. \quad (2.10)$$

Even though the latter term of Eq. 2.9 is of higher order in the perturbation theory, it usually has the same order of magnitude as the former. This can be understood from the previous discussion on the origin of various terms in Eq. 2.3,

and in particular what fields contribute to V_2 or V_3 . For this to be true, however, it is important that the orbitals u_n , and u_m in the second term have contributions that originate from an atom with a strong spin-orbit coupling. From the point of view of symmetries, another requirement for the second term to be nonzero is that u_n and u_m have contributions that have different parity, since \mathbf{p} is odd in spatial coordinates, $\mathbf{k} \cdot \mathbf{p}$ is only non-zero when one of the orbitals is odd with respect to a spatial direction and the other even. One example could be a p_y orbital and a $s-p_z$ hybridized one, which would be created by the ferroelectricity with electric polarization along the z -axis (add drawing? add hopping matrix?).

2.3 Orbital Rashba Effect

Unlike the purely relativistic Rashba-Bychkov effect, the orbital effect combines strong atomic SOC with the generation of nonzero orbital angular momentum (OAM) through electrostatic means. This contribution, therefore, is not limited by the small prefactors of Eq. 2.9. As will be explicitly shown below, electric dipole matrix element s can cause Bloch functions to acquire nonzero OAM when any electric field is present (e.g. from electric polarization), and vice versa Bloch functions with nonzero OAM acquire nonzero electric dipoles between unit cells [Petersen2000, Park2011, Go2016]. This leads to two separate effects.

Firstly, when atomic SOC is included, OAM is unquenched at the high symmetry k-points. This leads to a correction to the band dispersion that varies linearly with \mathbf{k} . Secondly, even without including the contribution of the atomic SOC, the OAM of the Bloch functions to appear in a chiral texture as one moves away from the high-symmetry k-point, similarly to how the relativistic Rashba effect leads to a chiral spin texture. If one then includes the atomic SOC from Eq. 2.3, this linear-in-k l will lead to a linear variation of the energy with either positive or negative slope, depending on the spin orientation.

We now proceed by giving a pedagogical derivation of this mechanism based on a tight-binding model [Petersen2000, Go2016].

2.3.1 Tight-Binding model

The tight-binding model is defined on a 2D square layer with lattice parameter a , one atom per unit cell, and four Wannier orbitals centered on that atom. These orbitals resemble the angular character of an s -orbital and three p -orbitals: $|s^n\rangle$, $|x^n\rangle$, $|y^n\rangle$, $|z^n\rangle$, where \mathbf{n} denotes the unit-cell indices (n_x, n_y) to which the Wannier function belongs to. To simplify notation, we omit $\mathbf{0}$ in writing the Wannier functions of the central unit cell. We furthermore assume that these orbitals have a Gaussian radial shape $\langle \mathbf{r}|s_{\mathbf{n}}\rangle = e^{-\frac{|\mathbf{r}-\mathbf{n}a|^2}{a^2}}$, $\langle \mathbf{r}|\alpha_{\mathbf{n}}\rangle = \alpha e^{-\frac{|\mathbf{r}-\mathbf{n}a|^2}{a^2}}$ with $\alpha = x, y, z$, and inner products implying integrals over space. The reason for choosing gaussians is to make solving the overlap integrals easier, changing to a different radial shape for the orbitals does

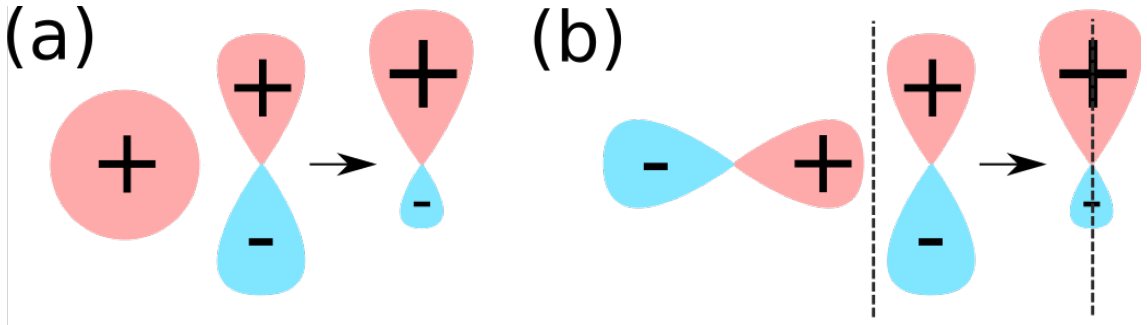


Figure 2.3: **Overlap dipoles.** (a) On-site dipole from $|s\rangle$ and $|z\rangle$ hybridization, (b) Dipole due to overlap of shifted $|p\rangle$ orbitals, the dashed line signifies a unit cell boundary.

not lead to any qualitative changes to the derivation below. The bare tight-binding Hamiltonian is denoted as \hat{H}_0 and includes the usual hopping parameters due to overlap $t_{\alpha\beta}^{\mathbf{n}\mathbf{n}'} = \langle \alpha^{\mathbf{n}} | \frac{\hat{\mathbf{p}}^2}{2m} + \hat{V} | \beta^{\mathbf{n}'} \rangle$. To mimick the inversion symmetry breaking in ferroelectric materials (i.e. with a polar space group), an electric field perpendicular to the layer (z direction) is applied. This allows extra hopping terms associated with $\hat{H}_{isb} = e(\hat{\mathbf{d}} \cdot \mathbf{E})$, with $\hat{\mathbf{d}}$ the electric dipole moment:

$$\langle s | \hat{H}_{isb} | z \rangle = 2eE_z\theta_z^0 \quad (2.11)$$

$$\langle z | \hat{H}_{isb} | x^n \rangle = eE_z\theta_z^n n_x \quad (2.12)$$

$$\langle z | \hat{H}_{isb} | y^n \rangle = eE_z\theta_z^n n_y \quad (2.13)$$

with $\theta_z^n = -ae^{-\frac{1}{2}\left(\frac{a|\mathbf{n}|}{a_0}\right)^2} \frac{\pi^{\frac{3}{2}}}{16\sqrt{2}}$, other terms of \hat{H}_{isb} are zero. Fig. 2.3 shows pictorially how these terms arise from the electric dipoles between the shifted orbitals. Since we are interested in ferroelectric materials, the internal field E_z caused by the electric polarization is usually small. This warrants a perturbative approach where \hat{H}_{isb} is the perturbation on \hat{H}_0 , leading to a hybridization between the $|s\rangle$ and $|z\rangle$ orbitals:

$$|\tilde{z}\rangle = |z\rangle + \frac{\langle s | 2eE_z\theta_z^n | z \rangle}{\varepsilon_z - \varepsilon_s} |s\rangle \quad (2.14)$$

$$|\tilde{s}\rangle = |s\rangle + \frac{\langle z | 2eE_z\theta_z^n | s \rangle}{\varepsilon_s - \varepsilon_z} |z\rangle, \quad (2.15)$$

where $\varepsilon_s = \langle s | \hat{H}_0 | s \rangle$ and $\varepsilon_z = \langle z | \hat{H}_0 | z \rangle$.

We can then write the kinetic energy part of \hat{H}_0 and terms of this hybrid $|\tilde{z}\rangle$ orbital in the central unit cell and the shifted $|x\rangle$, $|y\rangle$ orbitals, leading to:

$$\langle \tilde{z} | \hat{H}_0 | x^n \rangle = \frac{2eE_z\theta_z^n}{\varepsilon_z - \varepsilon_s} \langle s | \frac{-\nabla^2}{2} | x^n \rangle \quad (2.16)$$

$$= \frac{4eE_z(\theta_z^n)^2}{\varepsilon_z - \varepsilon_s} n_x (-5 + a^2|\mathbf{n}|^2) \quad (2.17)$$

$$\langle \tilde{z} | \hat{H}_0 | y^n \rangle = \frac{4eE_z(\theta_z^n)^2}{\varepsilon_z - \varepsilon_s} n_y (-5 + a^2|\mathbf{n}|^2) \quad (2.18)$$

To construct $\hat{H}_0^{\mathbf{k}}$ and $\hat{H}_{isb}^{\mathbf{k}}$, one can fourier transform the Wannier Functions following Eq. 1.14:

$$|\alpha^{\mathbf{k}}\rangle = \frac{1}{\sqrt{N}} \sum_{\mathbf{n}} e^{i\mathbf{k}\cdot\mathbf{n}} |\alpha^n\rangle \quad (2.19)$$

with $|\alpha\rangle$ one of the four aforementioned orbitals, \mathbf{k} written in terms of crystalline coordinates ($\frac{2\pi}{a}$), and N denoting the total amount of unit cells in the material. This results in:

$$\hat{H}_0^{\mathbf{k}} + \hat{H}_{isb}^{\mathbf{k}} = \sum_{\mathbf{n}} e^{i\mathbf{k}\cdot\mathbf{n}} (\hat{H}_0^n + \hat{H}_{isb}^n) \quad (2.20)$$

If we then assume that at $k = 0$ the Bloch functions are formed from p_x , p_y , \tilde{p}_z and \tilde{s} orbitals through Eq. 2.19, a perturbation theory for small deviations \mathbf{k} away from zero can be formulated as ($\mathbf{k} = 0$ superscripts are omitted for simplicity):

$$|\alpha^{\mathbf{k}}\rangle = |\alpha\rangle + \sum_{\beta \neq \alpha} \frac{\langle \beta | \hat{H}_0^{\mathbf{k}} + \hat{H}_{isb}^{\mathbf{k}} | \alpha \rangle}{\varepsilon_{\alpha} - \varepsilon_{\beta}} |\beta\rangle \quad (2.21)$$

Gathering the linear-in- k terms from the expansion of $e^{i\mathbf{k}\cdot\mathbf{n}}$ in Eq. 2.20, and assuming $\varepsilon_p = \langle x | \hat{H}_0 | x \rangle = \langle y | \hat{H}_0 | y \rangle$ at $\mathbf{k} = 0$, we find

$$|x^{\mathbf{k}}\rangle = |x\rangle + i\Theta \frac{k_x}{\varepsilon_p - \varepsilon_{\tilde{z}}} |\tilde{z}\rangle \quad (2.22)$$

$$|y^{\mathbf{k}}\rangle = |y\rangle + i\Theta \frac{k_y}{\varepsilon_p - \varepsilon_{\tilde{z}}} |\tilde{z}\rangle \quad (2.23)$$

$$|\tilde{z}^{\mathbf{k}}\rangle = |\tilde{z}\rangle + i\Theta \frac{1}{\varepsilon_{\tilde{z}} - \varepsilon_p} (k_x |x\rangle + k_y |y\rangle), \quad (2.24)$$

with $\Theta = \frac{\pi^{5/2}}{256a^3} \left(-16\sqrt{2} + \frac{3a\pi^{3/2}}{\varepsilon_z - \varepsilon_s} \right) eE_z$. Then, using the definition of the OAM operators for p -orbitals:

$$\hat{L}_x = \begin{pmatrix} 0 & 0 & 0 \\ 0 & 0 & -i \\ 0 & i & 0 \end{pmatrix}, \hat{L}_y = \begin{pmatrix} 0 & 0 & i \\ 0 & 0 & 0 \\ -i & 0 & 0 \end{pmatrix}, \hat{L}_z = \begin{pmatrix} 0 & -i & 0 \\ i & 0 & 0 \\ 0 & 0 & 0 \end{pmatrix} \quad (2.25)$$

we find that,

$$\langle \tilde{z}^{\mathbf{k}} | \hat{L}_x | \tilde{z}^{\mathbf{k}} \rangle = -2\Theta \frac{k_y}{\varepsilon_{\tilde{z}} - \varepsilon_p} \quad (2.26)$$

$$\langle \tilde{z}^{\mathbf{k}} | \hat{L}_y | \tilde{z}^{\mathbf{k}} \rangle = 2\Theta \frac{k_x}{\varepsilon_{\tilde{z}} - \varepsilon_p} \quad (2.27)$$

These expressions for \hat{L} can be filled into the expression for the atomic SOC $\hat{H}_{soc} = \lambda \hat{\mathbf{L}} \cdot \hat{\boldsymbol{\sigma}}$ to find the energy for $|\tilde{z}^{\mathbf{k}}\rangle$:

$$\varepsilon^{\mathbf{k}} = \frac{2\lambda\Theta}{\varepsilon_{\tilde{z}} - \varepsilon_p} (\mathbf{k} \times \boldsymbol{\sigma}) \quad (2.28)$$

which has the form of Eq. 2.1. We want to emphasize here that the only influence of the initial choice of the Gaussian radial shape of the orbitals is reflected in the prefactor in front of eE_z in the definition of Θ .

From this qualitative derivation, it is clear that the main reason behind the orbital Rashba effect can be traced back to the observation that Bloch functions with nonzero OAM have electric dipoles that couple to the inversion symmetry breaking electric field. We identified two sources that lead to the effect: the first one comes from the direct overlap dipoles between p_x and p_y orbitals, and the p_z orbital[Petersen2000], the second is due to the hybridization of the s and p_z overlap, and the kinetic energy term between the s and neighboring p_x and p_y orbitals[Go2016]. These two terms are reflected in the two terms that contribute to Θ , and lead to a chiral, linear-in- k texture of the OAM. If there then exists strong atomic SOC, this linear-in- k OAM will couple to the spin and result in the final Rashba-like form of Eq. 2.28.

There is one final term that contributes to the linear variation of OAM with \mathbf{k} , which is only present when there is an unquenching of the OAM at the high symmetry point ($|k| = 0$) due to the atomic SOC ???. This is due to the energy gain from \hat{H}_{soc} if the material has orbitals that have $\mathbf{j} = \mathbf{l} + \frac{1}{2}\boldsymbol{\sigma}$. Similar to the above derivation a small- k expansion for orbitals with nonzero OAM can be performed, leading in general to:

$$\langle \alpha | \hat{L}_\gamma | \beta \rangle = i\epsilon_{\alpha\beta\gamma} c_\alpha^* c_\beta \quad (2.29)$$

when α, β, γ designate x, y, z . This means that there has to be at least some admixing of multiple p -orbitals to get nonzero OAM. This leads to the following expansion of the Bloch functions around the high-symmetry $|k| = 0$ point:

$$|\psi(\mathbf{k})\rangle = \sum_{\mathbf{n}, \alpha} c_\alpha(\mathbf{k}) e^{i\mathbf{k} \cdot \mathbf{n}} |\alpha(\mathbf{n})\rangle \quad (2.30)$$

$$= \sum_{\mathbf{n}, \alpha} \left(c_\alpha(0) + \mathbf{k} \frac{\partial c_\alpha(\mathbf{k})}{\partial k} \Big|_{\mathbf{k}=0} \right) (1 + i\mathbf{k} \cdot \mathbf{n}) |\alpha(\mathbf{n})\rangle. \quad (2.31)$$

Focusing on the terms that vary linearly with k , the second term in the c expansion together with the first term in the exponent expansion is exactly the contribution that was discussed before. The final term for the Orbital Rashba effect originates from combining the first term in the c expansion with the second in the exponent expansion, leading to the contribution

$$\varepsilon(\mathbf{k}) = \langle \psi(\mathbf{k}) | \hat{H}_{isb} | \psi(\mathbf{k}) \rangle = i \sum_{\mathbf{n}, \alpha, \beta} c_\alpha^*(0) c_\beta(0) \mathbf{k} \cdot \mathbf{n} \langle \alpha(0) | \hat{H}_{isb} | \beta(\mathbf{n}) \rangle \quad (2.32)$$

$$= ieE_z \frac{-\pi^{5/2}}{8\sqrt{2}a^3} (c_x^*(0)c_z(0)k_x + c_y^*(0)c_z(0)k_y) \quad (2.33)$$

$$= eE_z \frac{\pi^{5/2}}{8\sqrt{2}a^3} (L_y(0)k_x - L_x(0)k_y). \quad (2.34)$$

These expressions show us that, due to $\hat{H}_{soc} = \lambda \hat{\mathbf{L}} \cdot \hat{\boldsymbol{\sigma}}$ and $\hat{H}_{isb} = eE_z d_z$, an additional Rashba-like term appears in the energy dispersion.

With the understanding that one can find Rashba like dispersions, coming not from the usually considered purely relativistic, but also from electrostatic mechanisms. We now look at a concrete example that behaves very similar to the above toy model, GeTe.

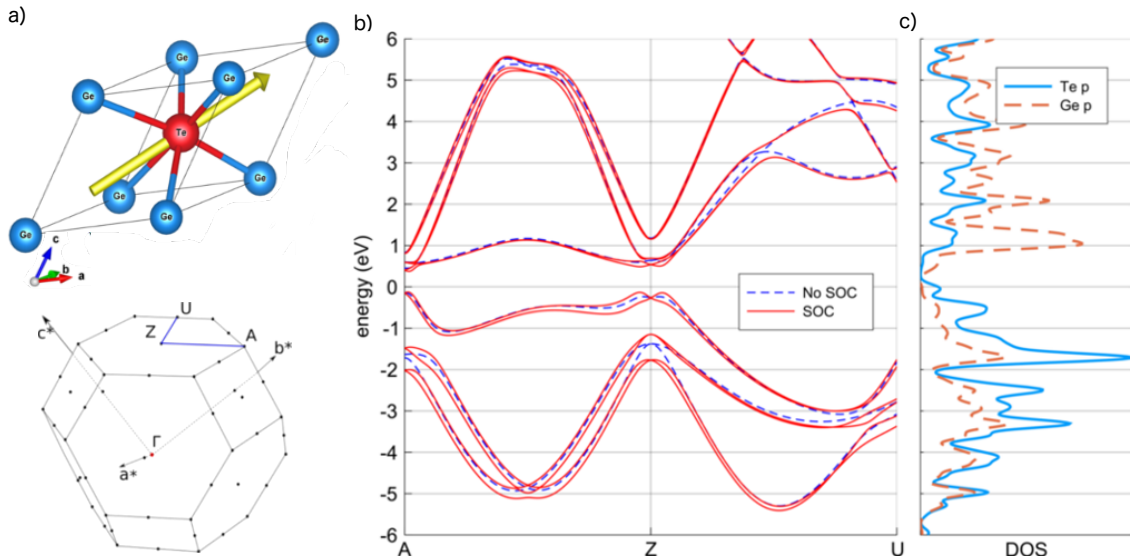


Figure 2.4: (a) Rhombohedral unit cell and Brillouin zone of GeTe, with the polarization direction in yellow. (b) Band structure obtained from a DFT calculation with and without SOC, along the blue path in panel (a). (c) partial DOS for Te and Ge p orbitals computed without SOC.

2.4 Overview: Germanium Telluride

The space group of GeTe is $R\bar{3}m$ (#160 in International Tables), with ferroelectric polarization along the threefold rotation z -axis caused by an off-centering of the central Te atom [Rabe1987] as displayed in Fig. 2.4-(a). The valence and conduction bands are formed mostly by s and p orbitals from Te and Ge, respectively. This, together with the large spin-splitting in the vicinity of the Z point [DiSante2013] as observed from the bandstructure in Fig. 2.4-(b), lends it as a perfect test-case for the above described mechanisms. Moreover, since it is a bulk material, the relativistic Rashba effects contribute negligibly due to the small potential gradients caused by bulk ferroelectricity. The band structure, presents a distinct large linear spin splitting around the Z point, along the $Z - A$ and $Z - U$ paths. The $Z - \Gamma$ path shows no splitting because the electric field is along the z direction, and as shown by the above derivation, only k_x and k_y will show a linear splitting. The density of states (DOS), displayed in Fig. 2.4-(c), confirms the orbital character of the bands.

2.5 Methods

We performed ab-initio DFT calculations using the Quantum-Espresso software package[[Giannozzi2009](#)]. In order to confirm the linear varying OAM even when spin-orbit is not included we performed non-relativistic, as well as fully relativistic calculations. Both were performed using ONCVPSP pseudopotentials, with 30 Ry for the energy cutoff, and 120 Ry for the density cutoff. The reciprocal space was sampled using a 6x6x6 Monkhorst-Pack grid, for the self-consistent and non self-consistent calculations, using an energy convergence threshold of 10^{-7} Ry. Afterwards we used the Wannier90 package [[Mostofi2014AnFunctions](#)] to perform the Wannierization, using projections on atomic *s*- and *p*-orbitals for both Ge and Te ions. The result is showcased in Fig. 2.5.

Since the present theory depends crucially on local, real space, properties of the Bloch functions, the next step is to generate the Wannier orbitals $|w_\alpha(\mathbf{r})\rangle$.

This provides us with the tools to analyze the real space properties of Bloch functions such as the dipole moment and OAM.

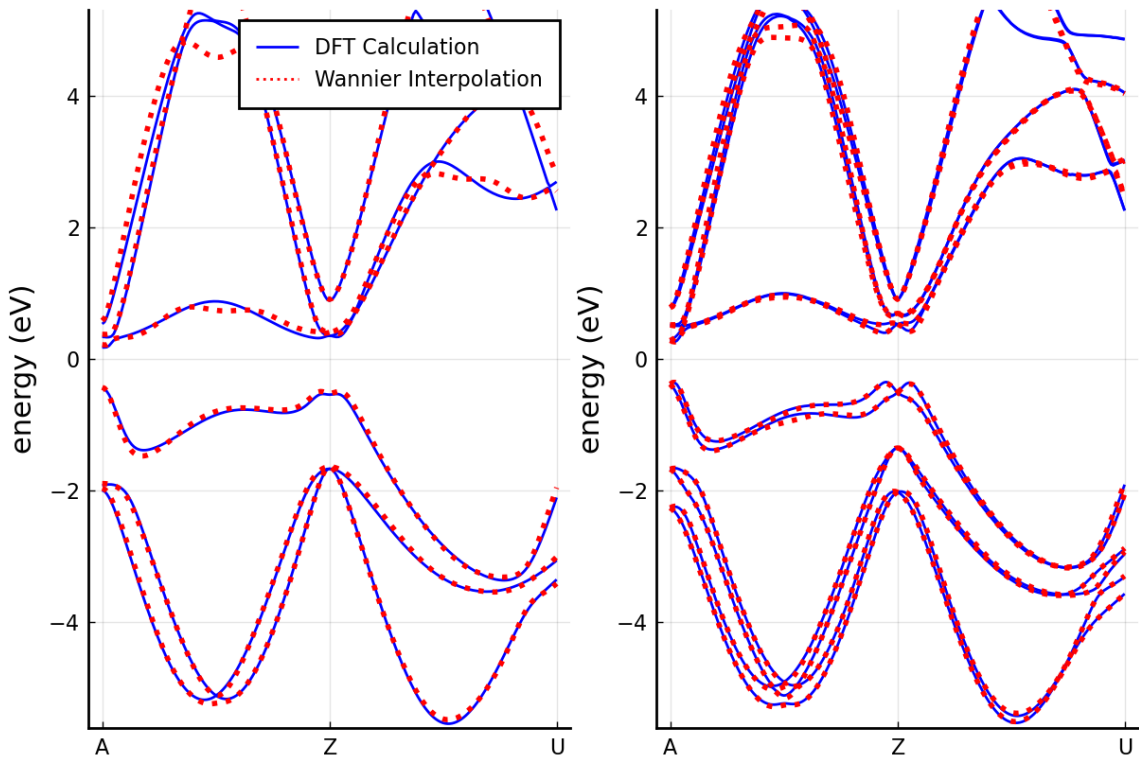


Figure 2.5: Result of Wannierization procedure for non-relativistic (a) and relativistic (b) calculations.

2.6 Band structure

The bands we will focus on most are the three topmost valence bands. As seen in Fig. 2.4-(b), these bands have the largest spin-splitting. This suggests that indeed the atomic SOC plays an important rule, seen as these bands are comprised mostly of Te orbitals, and SOC is largest on Te. If one were to fit the dispersion of the topmost band to Eq. 2.1, it results in a large prefactor $\alpha_R \approx 30.7 \text{ eV}\cdot\text{\AA}$ [DiSante2013]. As discussed before, a more realistic prefactor would be $\alpha_R = 10^{-6} \text{ eV}$ in the purely relativistic case inside the vacuum.

The last issue with the purely relativistic explanation, which has been confirmed

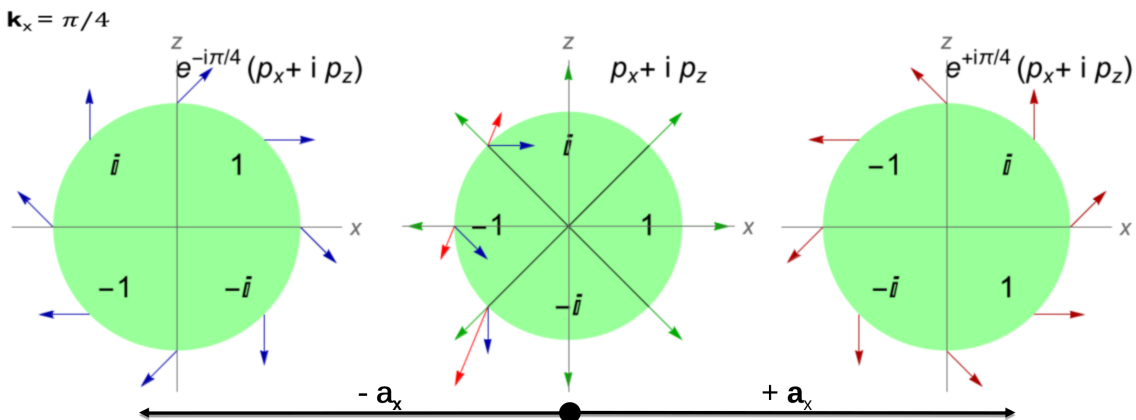


Figure 2.6: Interference between orbitals with nonzero OAM. Three neighboring unit cells are displayed, each with the same $p_x + ip_z$ orbital (thus having nonzero l_y). The wave functions of the left and right unit cells have their phase rotated by the plane-wave part $e^{ik_x R_x}$. The amplitude and phase of the wave function are encoded with the length and polar angle of the arrows.

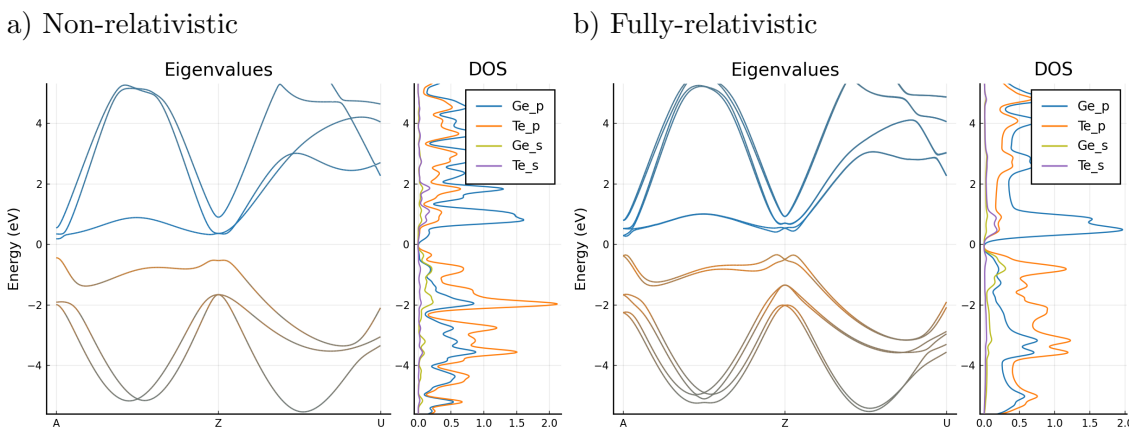


Figure 2.7: Bandstructure and projected density of states. In both panels the bandstructure was colored according to the contribution of the constituent orbitals, as indicated in the density of state plots. The bands that are formed by the s -orbitals are situated 5 eV below the shown window.

experimentally[Krempasky2015SurfaceSemiconductor], lies in the orientation of the spin polarization of the split bands. According to Eq. 2.1, the bands should all be split equally and Bloch functions at the same k -point should have the same spin orientations, since their character does not enter Eq. 2.1. However, as has been shown and will be confirmed by our results below, the orientation depends on the character of the band, more specifically on the value of the total angular momentum j .

2.7 Results and Discussion

The dispersion, OAM, and SAM of the first valence band are shown in the left panel of Fig. 2.8. Confirming our earlier conclusions, we can see that non-zero, linearly varying OAM is formed as we move away from the high-symmetry Z -point. Moreover, the OAM is perpendicular to both the z -axis and the k vector, as it should be from Eq. 2.26, and can also be seen from the panels in Fig. 2.10. This leads e.g. to $l_y = 0$ along the $A \rightarrow Z$ path, where only k_y is nonzero. When atomic SOC is included in the orange and blue graphs, we see the spin-splitting that results from having the spin oriented either along or opposite to the already linearly varying OAM. The unquenching of the OAM at the Z -point when SOC is included is also clearly visible, together with the resulting change in the slope that originates from the corresponding contribution to the dipole moment Eq. 2.32. This correlation can also be observed in the panel showing the center of mass $\bar{z} = \int_{\text{supercell}} z |\psi(k)|^2$ of the Bloch-functions, which is proportional to the dipole moment around the same reference point.

When we compare this first valence band with the third valence band, shown in the right panel of Fig. 2.8, we can clearly see the previously discussed issues with the purely relativistic explanation. As stated before, we can note that not only the magnitude but also the sign of the prefactor in Eq. 2.1 is opposite for these two bands, showcased by the size of the splitting, and by the ordering of the spin-up vs the spin-down splitted part. This is because the character of the first and third valence bands are different. The first valence band is mostly coming from Te $j_{\frac{3}{2}}$ orbitals, whereas the third valence band is predominantly $j_{\frac{1}{2}}$. This causes the orientation of the OAM and SAM to be along eachother in the first band, and opposite for the third, as shown in Fig. 2.10. This then leads to the different ordering of the spin-split bands.

There is one last very interesting feature one can notice from Fig. 2.10 (c) and (f), that is, the switching of the character (and SAM, OAM orientation) of the bands, very close to the Z point. This is because the crystal field breaks rotational symmetry causing the atomic j to not be a conserved quantity, i.e. there is a mixing between different atomic j orbitals, which varies strongly in this very narrow region around Z .

All these considerations lead to a very nontrivial SAM and OAM texture of the

bands as we progress through the BZ.

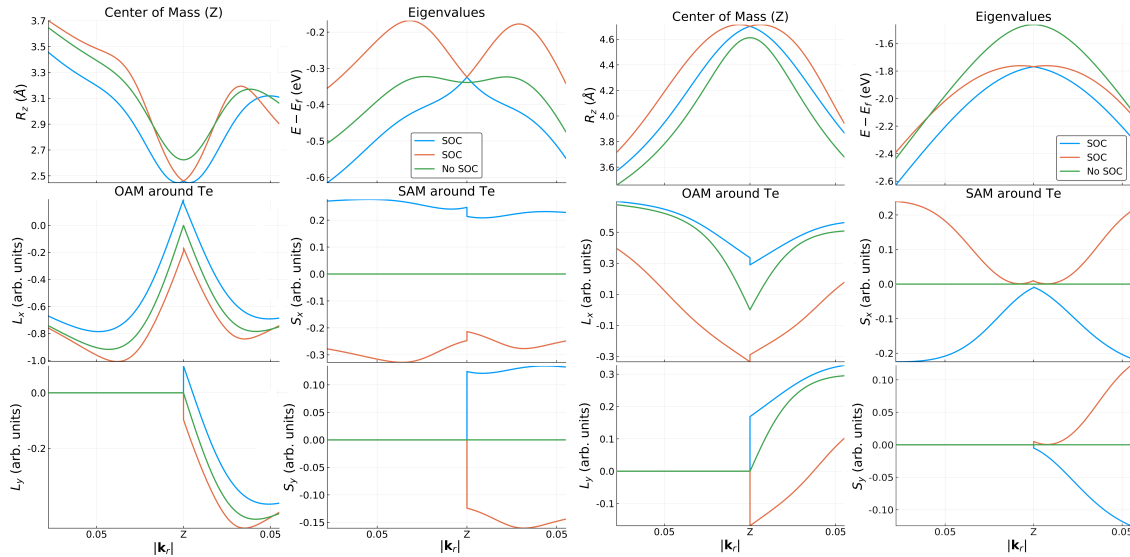


Figure 2.8: Comparison between the real-space observables and energy dispersion in (a) the first and (b) third valence band. The values are plotted in function of the relative distance from the Z point $\mathbf{k}_r = \mathbf{k} - \mathbf{k}_Z$, towards the A and U points. The green graphs denote the values before turning on atomic SOC, whereas the orange and blue graphs denote the two spin-split bands.

2.8 Conclusions

We have explored the microscopic origin of the giant Rashba-like spin splitting in the band structure of bulk ferroelectric GeTe with high atomic SOC. We derived the form of the band dispersion in the Wannier representation, that relates the large spin splitting to the intricate interplay between OAM, atomic SOC, the crystal field and the electric polarization. It turns out that the crucial component, which is not present in the relativistic Rashba effect, is the emergence of a nonzero electric dipole of the Bloch functions due to their OAM. The quantitative analysis based on Wannier functions and atomic-centered approximation confirms this mechanism in GeTe. We find a very good agreement between the proposed band dispersion, Eq. (??), and the dispersions of the first and third valence bands, where the effect manifests itself most clearly.

Ultimately, the results suggest that (1) large ferroelectric polarization, (2) high atomic SOC, and (3) highly symmetric environment producing little OAM quenching could be the design rules for new materials with strong Rashba-like spin splitting. These materials could enable spintronic devices with the much needed electric control of spin polarization.

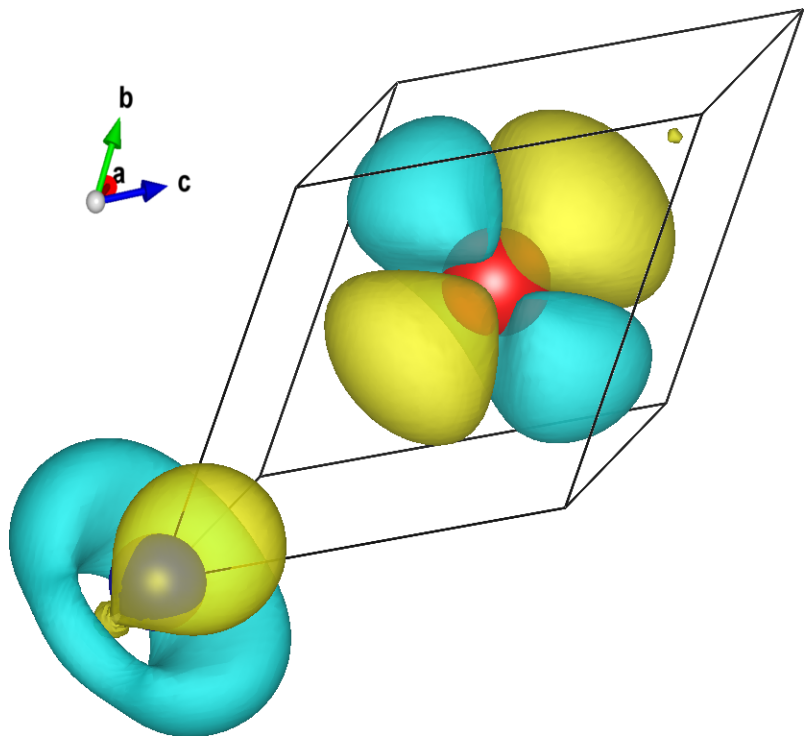


Figure 2.9: The variation of the charge density of the Bloch function of the first valence band $\frac{\partial|\psi(k)|^2}{\partial k}\Big|_{k=Z}$ away from Z towards A . Te and Ge ions are in red and blue, respectively. The charge asymmetry around Ge showcases the nonzero dipole moment along z , which couples to the local electric field near Ge ion.

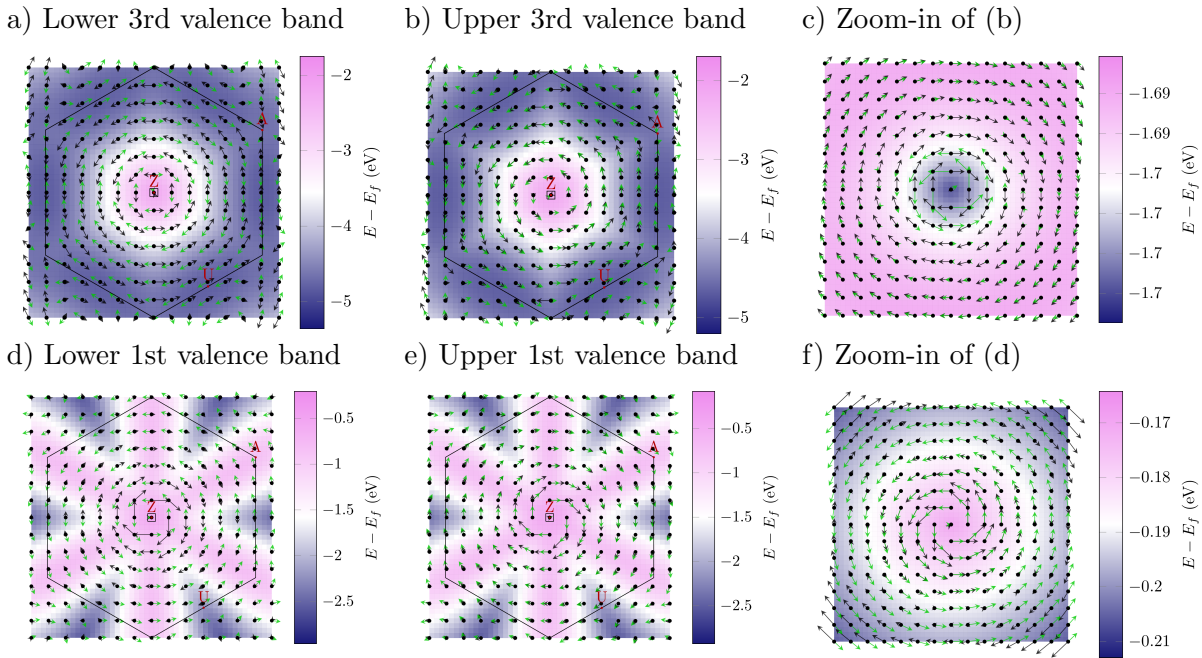


Figure 2.10: OAM and SAM textures around the Z point in the first and third valence bands of GeTe. The black and green arrows show the OAM and SAM textures, respectively. The length of the arrows was chosen separately for clarity in each figure and should thus not be compared. The color maps signify the energy of the bands, relative to the Fermi level. The small box around the Z point indicates the area, magnified in panels (c) and (f). In the zoomed figures (c) and (f) one can observe the change or relative orientation between the SAM and OAM when moving away from the Z point, signifying a change of character between $j = 1/2$ and $j = 3/2$.